RESEARCH ARTICLE

Key Points:
- A semiquantitative model explains the intensity variation of a moving red line cusp aurora
- A moving red line cusp aurora does not have electron precipitation in its rear half
- The velocity of the electron precipitation region is important for determining how the red line aurora extends horizontally

Horizontal profile of a moving red line cusp aurora

S. Taguchi[1] ⓘD, Y. Chiba[2], K. Hosokawa[2,3] ⓘD, and Y. Ogawa[4,5] ⓘD

[1]Department of Geophysics, Graduate School of Science, Kyoto University, Kyoto, Japan, [2]Department of Communication Engineering and Informatics, University of Electro-Communications, Tokyo, Japan, [3]Center for Space Science and Radio Engineering, University of Electro-Communications, Tokyo, Japan, [4]National Institute of Polar Research, Tokyo, Japan, [5]Department of Polar Science, SOKENDAI (Graduate University for Advanced Studies), Kanagawa, Japan

Abstract Auroral emission at a wavelength of 630.0 nm (red line) has a long radiative time. In this study, we show how this long radiative time controls the horizontal extent of a moving mesoscale aurora, which is typical of the cusp. Using high time resolution (4 s) observations by an all-sky imager at Longyearbyen, Svalbard, and observations by the European Incoherent Scatter Svalbard Radar (ESR), we examined the auroral emission enhancements obtained in the cusp during an interval of southward interplanetary magnetic field on 27 November 2011. Simultaneous observations from the all-sky imager and the ESR clearly show the manner in which auroral emission regions passed through the radar's field of view. When the front edge of the moving auroral structure intersected the radar's field of view, the ESR electron temperature was enhanced. A few minutes later, the ESR electron temperature dropped to the background level, indicating that the mesoscale electron precipitation region shifted away from the radar's field of view. At that time, the auroral emission in the radar's field of view decreased but still had adequate intensities. These results provide evidence demonstrating that moving cusp auroral emission occurs behind the electron precipitation region as well as inside that region. We interpreted this feature semiquantitatively by using the equation of continuity of the density of the excited atomic oxygen. Our model indicates that the maximum intensity in the moving auroral structure occurs at a point along the trailing edge of the electron precipitation region and that the velocity of that region is important for determining how the 630.0 nm aurora emissions extend horizontally.

1. Introduction

A moving mesoscale aurora at a wavelength of 630.0 nm (red line) is a typical phenomenon in the dayside cusp of the high-latitude ionosphere [e.g., *Sandholt et al.*, 1986, 1990; *Lockwood et al.*, 1989; *Fasel*, 1995] and is thought to be caused by enhanced fluxes of soft magnetosheath electrons in the moving flux tube driven by intermittent reconnection, i.e., a flux transfer event [*Haerendel et al.*, 1978; *Russell and Elphic*, 1978]. The latitudinal motion of the moving red line cusp aurora typically has velocities ranging from $0.5 \, \text{km s}^{-1}$ to $1 \, \text{km s}^{-1}$ and occasionally up to $1.5 \, \text{km s}^{-1}$ [e.g., *Vorobjev et al.*, 1975; *Sandholt et al.*, 1990]. This motion can be even faster in the longitudinal direction [e.g., *Lockwood et al.*, 1989; *Sandholt et al.*, 1990; *Moen et al.*, 1995; *Suzuki et al.*, 2008; *Taguchi et al.*, 2009]. The moving red line cusp aurora typically has a latitudinal extent of 100–200 km [e.g., *Sandholt et al.*, 1986, 1990] and sometimes has a shorter extent of ~50 km [e.g., *Sandholt et al.*, 1990; *Oksavik et al.*, 2004; *Taguchi et al.*, 2012].

Most of the aforementioned studies are based on the results of an all-sky imager, which is a powerful tool for obtaining information on the two-dimensional extent of the moving electron precipitation region. This feature is important for examining the evolution of the reconnected flux tube. The data obtained by a spacecraft at ionospheric heights would simply reflect the spatial structure inside the particle precipitation region without providing any information on its evolution. The extent of the moving red line aurora roughly agrees with the extent of the soft electron precipitation region. To obtain more detailed relationships between these two regions, we need to consider that the red line aurora is not prompt emission.

The red line emission originates from $O(^1D)$ atoms. Theoretically, the $O(^1D)$ state has a lifetime of 110 s. Moreover, its lifetime is reduced to 30–80 s at the typical altitude of the aurora, i.e., 250–300 km [e.g., *Sipler and Biondi*, 1972], owing to the quenching of $O(^1D)$ by its reactions with N_2, O_2, and O. When $1 \, \text{km s}^{-1}$ is taken as the typical speed of the moving cusp auroral structure, any effect from the relatively long lifetime of 30–80 s at the typical altitude of the 630.0 nm aurora might be seen across horizontal distances of 30 km

(= 1 km s^{-1} × 30 s)–80 km (= 1 km s^{-1} × 80 s). These distances are not negligible when the mesoscale structure of the moving cusp aurora is considered.

By examination of a moving cusp aurora structure with a typical horizontal scale of roughly 100 km × 200 km, *Taguchi et al.* [2015a] indicated that the maximum 630.0 nm intensity of the auroral structure occurs immediately behind the moving *F* region-enhanced electron density volume created by precipitating electrons. This indication is based on the delay of the auroral intensity peak of approximately 40 s from the peak of the electron density [*Taguchi et al.*, 2015a, Figures 8a and 8b]. This delay time is consistent with the lifetime of O(^{1}D), which suggests that the spatial relationship obtained by *Taguchi et al.* [2015a], such that the maximum 630.0 nm intensity in the cusp auroral structure is located immediately behind the enhanced electron density volume created by the precipitating electrons, is related to the relatively long lifetime of O(^{1}D). The aurora structure analyzed in *Taguchi et al.* [2015a], however, was not a completely isolated auroral event as explicitly stated in the paper. The data obtained after time 7, as shown in their Figure 8a, reflect variations associated with a different moving auroral structure that appeared immediately after the auroral structure examined in that paper. More detailed relationships of the 630.0 nm auroral emission region extension from the electron precipitation region need to be clarified.

In the present paper, we examine multiple events of isolated moving cusp aurora by using aurora image data having higher time resolution than those used in *Taguchi et al.* [2015a]. Moreover, we investigate plasma data from the European Incoherent Scatter (EISCAT) Svalbard radar (ESR), in which the beam passes through the moving auroral structure. On the basis of the ESR and auroral intensity data, we show the larger horizontal extension of the moving cusp aurora compared with the electron precipitation region, and we interpret the characteristics of its horizontal extension in terms of the equation of continuity of the density of the excited atomic oxygen.

2. Instrumentation

The instrumentation used in this study consists of a ground-based all-sky imager and ESR. The all-sky imager uses an electron multiplier charge-coupled device (EMCCD) camera (Hamamatsu, C9100-13) with an imaging resolution of 512 × 512 pixels, and it measures emissions at two wavelengths: 557.7 nm and 630.0 nm. The imager has been operating in Longyearbyen, Norway (geographical latitude 78.1°N and longitude 16.0°E) since October 2011 [*Taguchi et al.*, 2012]. During the first observation season, from October 2011 to February 2012, we obtained 630.0 nm data at 4 s intervals with an exposure time of 4 s per image. In the present study, we focused on events that occurred on 27 November 2011, during the first observation season; information after the second season or later has been reported elsewhere [*Taguchi et al.*, 2015a, 2015b]. We note that the imager can clearly detect faint emissions from polar cap patches in this exposure time [*Hosokawa et al.*, 2013a, 2013b, 2016a, 2016b; *Sakai et al.*, 2014]. For ESR, we used data from the 42 m dish antenna, which was fixed so that its beam was aligned with the magnetic field lines. In the following sections, we compare the plasma data averaged over the *F* region along the magnetic field lines with the 630.0 nm aurora intensity data obtained in the same direction.

3. Observations

3.1. Overview of Events Occurring on 27 November 2011

Figure 1 shows an example of the 630.0 nm all-sky images. This image was captured at 0747:02 UT, when Longyearbyen was located at approximately 1045 magnetic local time. The white arrow in the figure indicates a mesoscale elongated auroral structure, which is one of the events examined in this study. This aurora is located roughly along the geographical east-west meridian. The black diamond on the image of the aurora structure represents the direction of the ESR beam. As discussed subsequently, the aurora structure moved west-northwestward; at the same time, the ESR beam passed through the moving aurora structure.

This mesoscale aurora is among seven cases investigated in this study. Before providing the detailed characteristics of all of these events, we will provide aurora overviews in a keogram format during a longer interval together with the near-Earth interplanetary magnetic field (IMF) data. Figure 2 shows the north-south keogram reproduced from all-sky images for 0500–0900 UT and the IMF observations by the Geotail spacecraft. The black triangle shown at the bottom of Figure 2d indicates the time of the all-sky image data
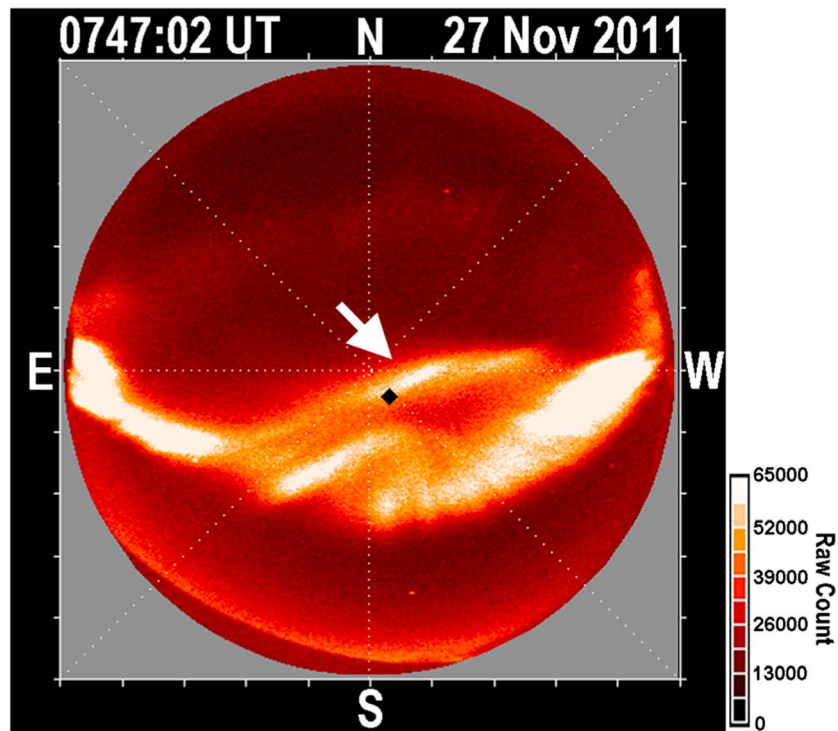
Figure 1. A 630.0 nm all-sky image taken at 0747:02 UT on 27 November 2011. A white arrow indicates a mesoscale auroral structure, which is one of the events examined in this study. A black diamond represents the direction of the ESR field-aligned radar beam. N-S and E-W represent the geographical north-south and east-west meridians, respectively.

shown in Figure 1 (0747:02 UT). During an interval from approximately 0600 to 0810 UT, the equatorward boundary of the aurora was located at the south at zenith angles larger than 30°, and many poleward moving aurora features were identified. On that day, the ESR 42 m radar began observations at ~0702 UT. In this study, we focus on the interval of approximately 1 h, from 0702 UT to 0800 UT.

Figures 2a–2c show the X_{GSM}, Y_{GSM}, and Z_{GSM} components of IMF data (15 s average) obtained by Geotail, respectively. The Geotail position during this 4 h interval is $(X_{GSE}, Y_{GSE}, Z_{GSE}) = (22.7–22.9, 9.6–12.4, −3.8$ to $−3.0) R_E$. No time lag was considered in the plot. The Z_{GSM} component, i.e., B_Z (Figure 2c), became negative after ~0605 UT, and the negative B_Z continued until ~0800 UT. A comparison of Figure 2c with Figure 2d reveals that the equatorward boundary of the aurora was situated to the south in accordance with the negative B_Z intervals, which reaffirms that the time lag from the Geotail to the cusp need not be introduced in this interval.

The Y_{GSM} component, B_Y (Figure 2b), had small magnitudes and predominantly negative values during 0500–0600 UT. Later, B_Y became positive. The X_{GSM} component of the IMF, B_X (Figure 2a), was positive except for a brief interval at nearly 0600 UT. During the plotted interval, the Wind spacecraft was also observing the IMF and solar wind at a distant upstream location. In the Wind IMF data, which are obtained from the NASA CDAWeb service, negative B_Z intensification accompanied with the change of the B_Y sign from negative to positive is evident at 0517 UT, which is 48 min ($= 0605$ UT $− 0517$ UT) before the similar change at Geotail. The Wind solar wind speed during 2 h after 0517 UT was roughly stable at 350 km s^{-1}. The proton density was between ~7 cm^{-3} and ~12 cm^{-3} for that period.

3.2. Simultaneous Observations From All-Sky Imager and ESR

Figure 3 shows the 30 s integrated electron density (N_e) and electron temperature (T_e) measured by ESR and the 4 s resolution aurora intensity (630.0 nm) obtained in the direction of the radar beam during 0700–0800 UT. Figures 3a and 3b represent the height profiles of N_e and T_e, respectively, and in Figure 3c, the auroral intensity (black dot) is compared with T_e (red line). T_e in Figure 3c represents the average value
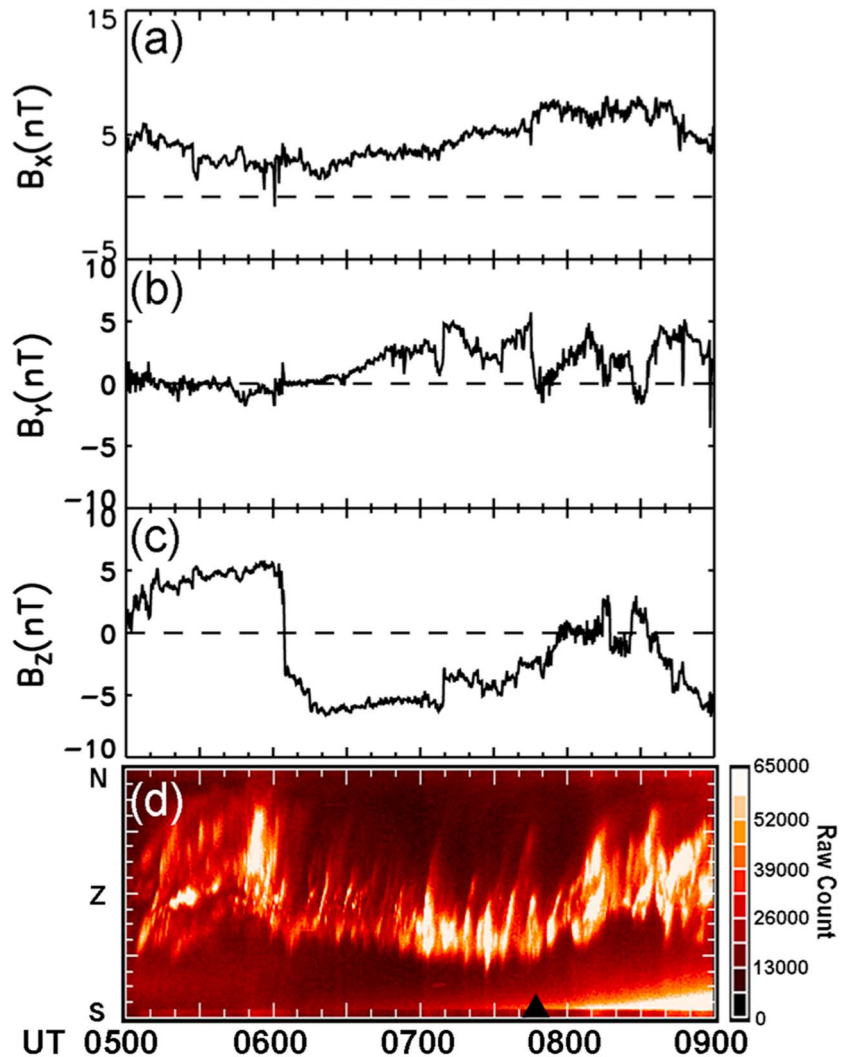
Figure 2. IMF observed by the Geotail spacecraft and 630.0 nm auroral intensity in the north-south keogram for 0500–0900 UT on 27 November 2011. The (a) X, (b) Y, and (c) Z components of the IMF in the GSM coordinate are plotted. (d) The keogram is reproduced from all-sky images. The black triangle shown at the bottom of Figure 2d indicates the time of the all-sky image data shown in Figure 1 (0747:02 UT).

from altitudes of 225–375 km. The error bars of this plot represent the standard deviation. The red horizontal line indicates $T_e = 2500$ K for reference. Figure 3d shows the average N_e values from altitudes of 225 km to 375 km (red) together with those from altitudes of 400 km to 500 km (blue). The error bars represent the standard deviation. The black dotted line indicates $N_e = 3 \times 10^{11}$ m^{-3} for reference. The black triangle in each panel represents the time (i.e., 0747:02 UT) at which the all-sky image shown in Figure 1 was captured.

We focused on the isolated auroral enhancements. In Figures 3c and 3d, the vertical solid line represents the start of the auroral enhancements. We determined the start as the time at which an increase occurred after a "quiet" interval that is longer than 4 min (240 s). Specifically, the auroral intensity exceeded the average for the preceding 240 s by at least 150 R, and the average from the following 16 s exceeded that auroral intensity by at least 150 R. We required an auroral intensity increase of more than 300 R for 20 (= 4 + 16) s.

Events 1–7 began at 0702:05, 0714:24, 0719:29, 0727:10, 0736:27, 0744:51, and 0755:07 UT, respectively. The aurora shown in Figure 1 is referred to as Event 6. In Event 6, as well as in Events 1, 5, and 7, the aurora
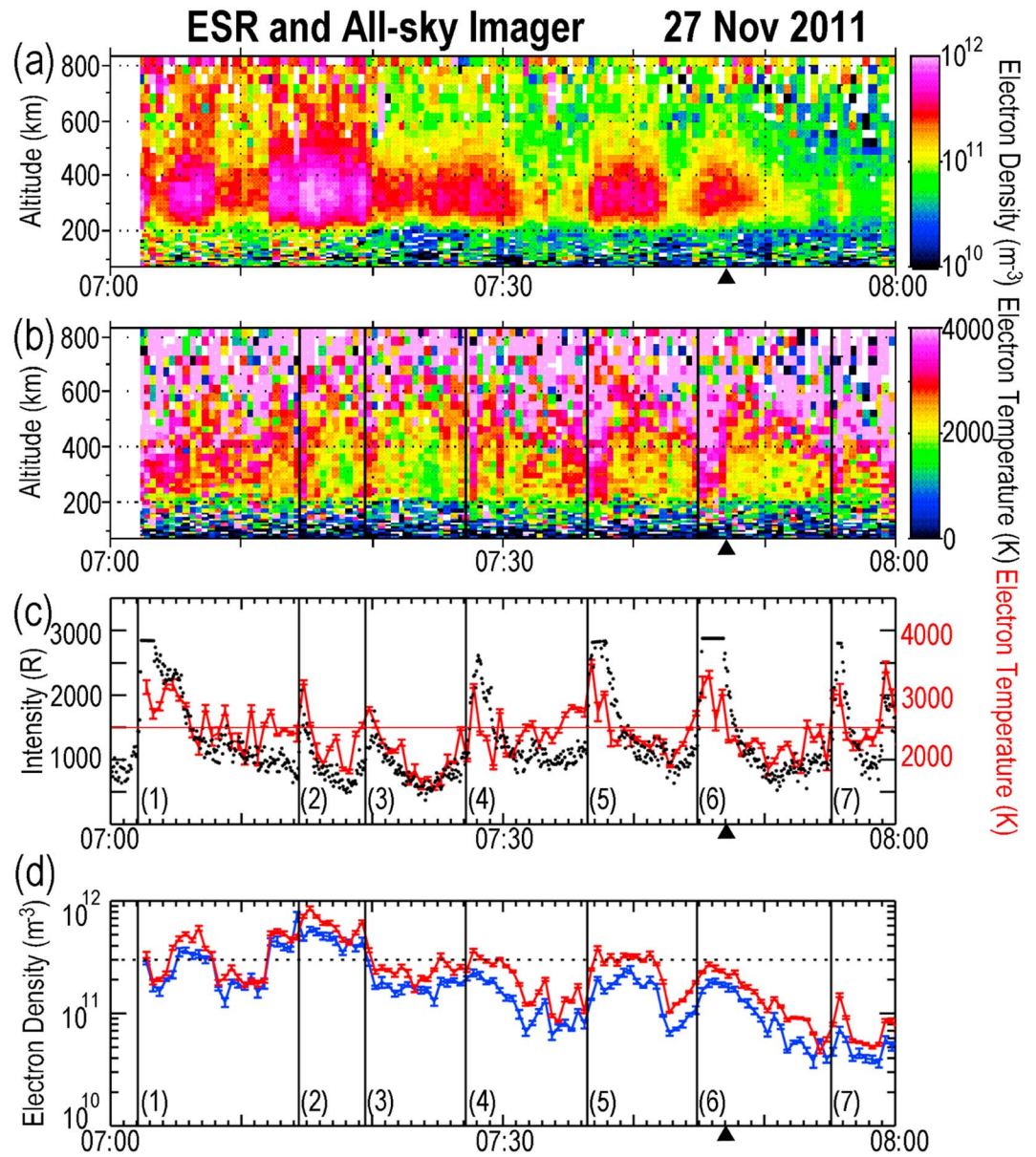
Figure 3. Electron density and electron temperature measured by ESR, and aurora intensity (630 nm) obtained in the direction of the ESR beam during 0700–0800 UT. The height profiles of (a) electron density and (b) electron temperature are presented. (c) The auroral intensity (black dot) and its comparison with the average T_e from a section 150 km in width centered at 300 km; i.e., 225–375 km is shown. The red horizontal line indicates $T_e = 2500$ K. (d) The average values of electron density from altitudes of 225–375 km (red) and those from altitudes of 400–500 km (blue) are plotted. The horizontal dotted line represents a reference value of 3×10^{11} m^{-3}. The seven vertical lines, shown as (1) to (7) in Figures 3c and 3d represent the start of the auroral enhancements. Those times are also shown in Figure 3b with the vertical lines except for (1). The black triangles in Figures 3a–3d represent the time (i.e., 0747:02 UT) when the all-sky image shown in Figure 1 was captured.

intensities (black dots) showed unusually constant features for a brief interval. These features mean simply that the aurora intensity exceeded the upper limit of the dynamic range of the EMCCD camera in the observation mode used in that season. For all events except for Event 1, the start time is also shown in Figure 3b, as represented by the vertical line.

Figure 3b shows that at the start of Event 6 (second vertical line from the right) the ESR T_e at altitudes near 300 km was sharply enhanced (reddish color, roughly 3000 K). Similar features were observed in Events 2–5 and 7, although for Event 5, the T_e enhancements appeared to start gradually a few minutes earlier than

Table 1. Auroral Intensity at the Time of T_e Drop

Event	UT for $T_e < 2500$ K	I_{MAX} (R)	I_{MIN} (R)
1	0706:00–0706:30	1700	1300
2	0715:30–0716:00	1000	800
3	0720:30–0721:00	1300	1000
4	0728:00–0728:30	2600	2000
5	0738:00–0738:30	2400	1800
6	0747:00–0747:30	2400	1700
7	0756:00–0756:30	2400	1500

the start time of the auroral enhancements. These correlations between the start of T_e enhancements at altitudes near 300 km and the auroral intensity enhancements indicate that both have a common source: cusp electron precipitation. *Watermann et al.* [1994] showed that an electron temperature maximum of about 3000 K at altitudes of ~300 km is well explained by cusp electron precipitation. We obtained the average T_e from a section 150 km in width centered at 300 km, i.e., 225–375 km. The temporal variations are shown in Figure 3c.

Figure 3c shows that at the start of Event 6 the ESR T_e was enhanced and exceeded 2500 K. Between 0745:30 and 0746:00 UT, T_e reached its maximum value of approximately 3300 K. In this 30 s interval, the auroral intensity was also strong, although its actual value was not measured. In all events except for Event 3, T_e exceeded 3000 K (Figure 3c), and the auroral intensity was also relatively strong (>2000 R) at each T_e maximum.

We now examine the relationship between the drop in T_e and the decrease in auroral intensity. Figure 3c shows that for Event 6, T_e dropped below 2500 K between 0747:00 and 0747:30 UT. This drop is also clearly shown in Figure 3b as a sharp change in T_e at altitudes near 300 km (reddish color to yellow color). The auroral emission decreased during this 30 s interval but still had adequate intensities at ~1700 R to ~2400 R. These values are well above the background level. In Table 1, we summarized the auroral intensities observed when T_e dropped below 2500 K for all events. I_{MAX} and I_{MIN} in the table represent the maximum and minimum auroral intensity during the 30 s interval. For Events 4–7, I_{MAX} was 2400 R or more, and I_{MIN} was at least 1500 R, indicating that the auroral intensities were well above the background level. That is, the auroral emissions continued with adequate intensities even after T_e dropped below 2500 K. For the three other events (Events 1–3), the auroral intensities were relatively weak.

In Figure 3d the average N_e values from altitudes of 225 km to 375 km (red) show that the N_e variation at the start time differed among six events. In Event 2 N_e increased to a relatively high value (~9 × 10^{11} m^{-3}), whereas N_e decreased for Event 3. In Event 4, the N_e increase was not very prominent but that for Event 5 and Event 7 was clear. For Event 5, the enhanced N_e continued for a much longer time than the enhanced T_e (Figure 3c). For Event 6, the N_e increase was very gradual and did not reach 3 × 10^{11} m^{-3}. These inconsistencies suggest that the dominant N_e increase does not have a common source for the auroral emission intensification, i.e., electron precipitation except for Event 7. For Event 7 modest N_e enhancements correlated with enhancements of both T_e and the auroral intensity. N_e peaked at approximately 1.5 × 10^{11} m^{-3} during 0755:30–0756:00 UT in accordance with the T_e enhancements. This modest increase in N_e may have been caused by the ionization due to electron precipitation.

The most enhanced N_e occurred between Events 2 and 3. This interval clearly includes the period in which both T_e and the auroral intensity were very low (~0716 to ~0718 UT). For Event 5, relatively high N_e continued to ~0742 UT; the latter half of that enhanced N_e interval included the period in which both T_e and the auroral intensity were low. In general, the high N_e and low T_e observed in the cusp indicate that the plasma was transported to that region without being produced by an electron impact. Because IMF B_Z was southward (Figure 2), it is inferred that the high N_e and low T_e plasma arrived at the cusp from its equatorward side [e.g., *Lockwood and Carlson*, 1992]. In the present event, the N_e enhancements would not be a good indicator of the electron precipitation, as is the event presented by *Doe et al.* [2001].

Red line emissions can also be caused by thermal electron gas of sufficiently high temperature [e.g., *Rees and Roble*, 1975; *Kozyra et al.*, 1990; *Lockwood et al.*, 1993; *Carlson et al.*, 2013]. Those studies indicated that emission owing to thermal excitation is relatively strong when T_e is elevated to typically >3000 K and that N_e is relatively high (>3 × 10^{11} m^{-3}). Figures 3c and 3d (red lines) show that T_e and N_e at altitudes of ~300 km exceeded 3000 K and 3 × 10^{11} m^{-3}, respectively, only for three brief periods for Events 1, 2, and 4. Figure 3b shows that T_e often exceeded 3000 K at altitudes of 400–500 km, which is thought to be the dominant source for thermal excitation [*Lockwood et al.*, 1993; *Carlson et al.*, 2013]. However, Figure 3d indicates that
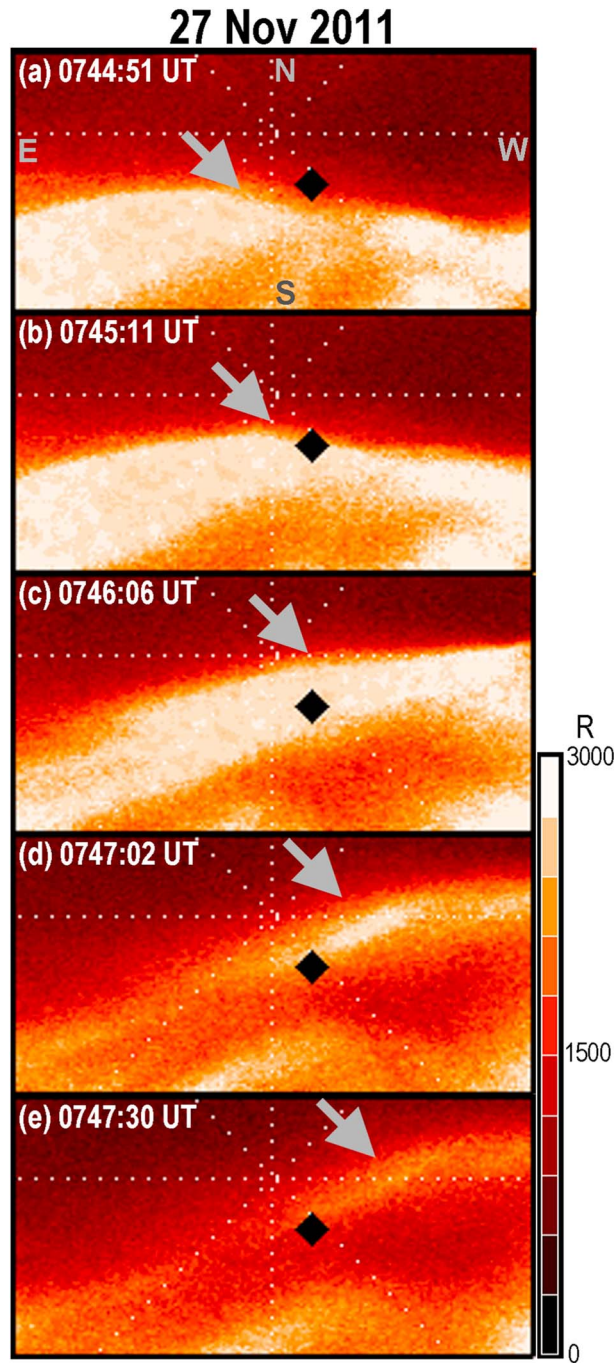
Figure 4. Auroral images at (a–e) five times during Event 6, representing that a mesoscale auroral structure was passing through the radar's field of view (black diamond). The gray arrow indicates the moving auroral structure. N-S and E-W in Figure 4a represent the geographical north-south and east-west meridians, respectively.
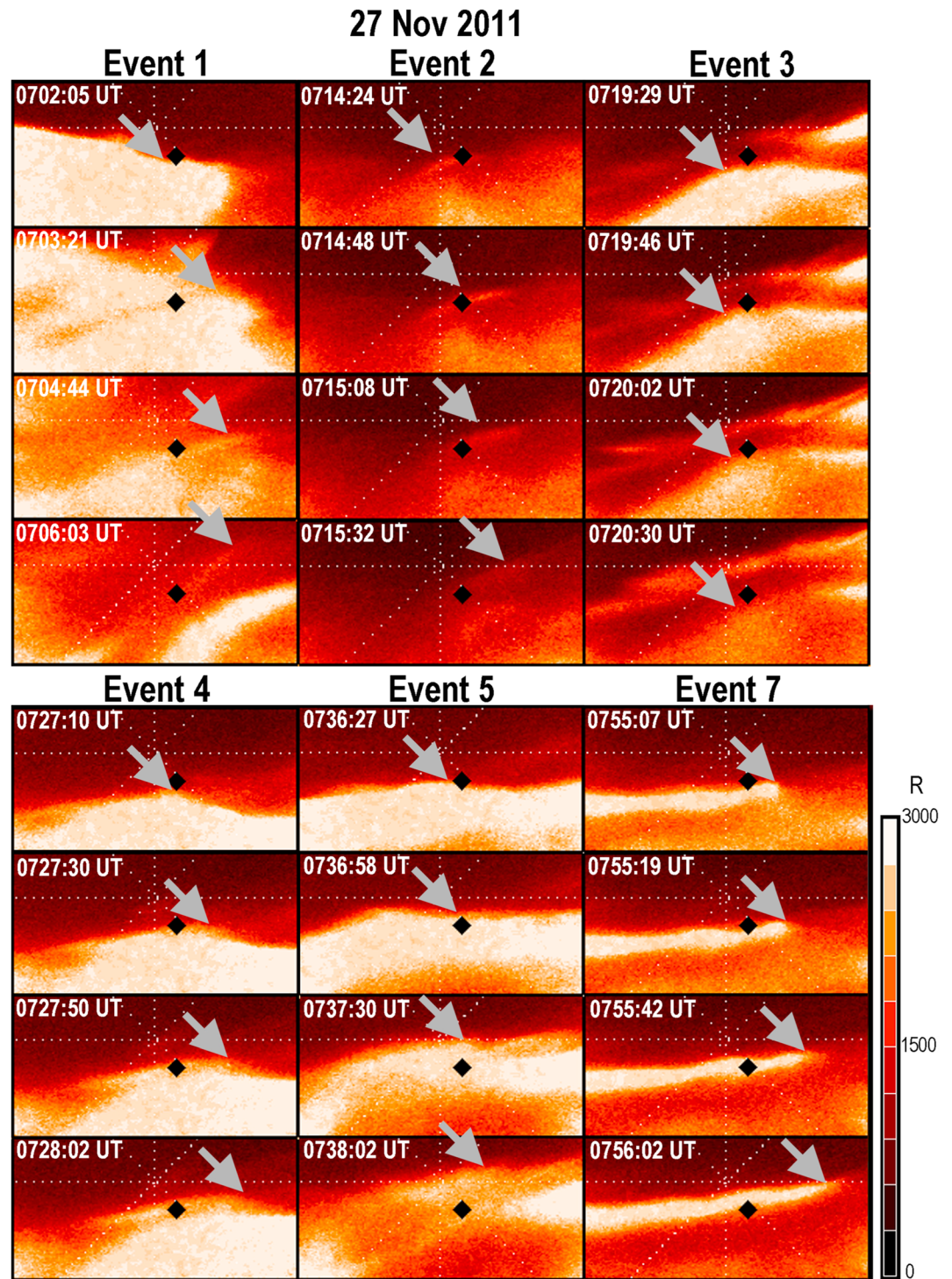
N_e at those altitudes (blue line) is below $3 \times 10^{11}\,\mathrm{m}^{-3}$ except for two brief intervals after Event 1 and between Events 2 and 3. During those brief intervals, the red line emission was not markedly high. Relatively strong red line emissions occurred in Events 5 and 6. For the 1 h interval investigated in this study, the contribution to the red line intensity from the thermal excitation was very small.

3.3. Motion of the Aurora in Seven Events

In Figure 4, five close-up auroral images around the radar's field of view are shown for Event 6. The black diamond in Figures 4a–4e indicates the direction of the radar's field of view. The auroral image in Figure 4a was obtained at 0744:51 UT, i.e., at the start of the auroral enhancements, as defined in Figure 3c. At the bottom left of this image, a relatively strong emission region is apparent, the northern boundary of which is indicated by the gray arrow. This auroral structure moved west-northwestward, and at 0745:11 UT (Figure 4b), the front part of the strong emission region intersected the radar's field of view. The west-northwestward motion in the northern cusp is consistent with IMF B_Y positive (Figure 2b).

At 0746:06 UT (Figure 4c), the radar's field of view passed through the central part of the auroral structure. Figure 4d is the first image obtained during the 30 s interval (0747:00–0747:30 UT in Table 1) in which the ESR T_e dropped below 2500 K. Such a low T_e implies the absence of significant electron precipitation in the direction of the radar's field of view. The radar's field of view passed through the rear part of the auroral structure at that time. Figure 4e shows the last image captured during the above mentioned 30 s interval (0747:30 UT). The radar's field of view was still passing through the rear part of the diminishing auroral structure. From these five images, the variations of the auroral intensity and T_e, shown in Figures 3b and 3c, have been inferred to be directly associated with the passage of the mesoscale auroral structure. Animation S1 in the supporting information shows the motion of the aurora for a longer period.

Figure 5. Motion of the auroral structure for six events, shown in the same format as that in Figure 4 except that each event has four images.

Four close-up auroral images for each of the other six events are shown in Figure 5. The format of each image is the same as that in Figure 4. The topmost image for each event was obtained at the defined start time of the auroral enhancements (time for the vertical lines in Figure 3c). The images in the second and third panels in each event indicate two situations that occurred after the start of auroral enhancements and before the ESR T_e drop to <2500 K. The image obtained immediately after the ESR T_e drop to <2500 K is shown at the bottom of the image stack for each event.

The top image for Event 1 shows that the strong aurora (gray arrow) existed immediately on the equatorward side of the radar's field of view at that time. A comparison of the top and the second images (0702:05 and 0703:21 UT) reveals that the start of the auroral enhancements in the radar beam direction was caused by the expansion and subsequent motion of the aurora located on the equatorward side. Figure 3c shows that at 0703:21 UT the auroral intensity in the radar beam direction was in its decreasing phase. From the image taken at 0703:21 UT (Figure 5), it is inferred that the ESR's beam was passing through the weak intensity region that was roughly aligned west-northwestward (gray arrow). Then, when the weakening of the auroral intensity was prominent on the northern side, such that at 0704:44 UT the radar's field of view was near the edge of the narrow aurora extending westward (gray arrow). This part of auroral structure moved northward until 0706:03 UT, when the radar's field of view was near the trailing edge of the diminishing aurora. From these images, we can infer that the auroral motion in the radar's field of view during Event 1 was complicated and that the variations in the auroral intensity in the direction of the radar's field of view (Figure 3c) are not the result of simple motion of a mesoscale auroral structure.

The four images (0714:24–0715:32 UT) for Event 2 show that the motion of the narrow auroral structure (indicated by the gray arrow) is associated with the auroral intensity in the radar's field of view. The auroral structure moved in the west-northwest direction, which is similar to the auroral structure for Event 6 (Figure 4). In the case of Event 3, the manner in which the auroral structure passed through the radar's field of view differed significantly from that shown in Event 6. A comparison of the topmost and the second images (0719:29 and 0719:46 UT) reveals that the start of the auroral enhancements in the radar beam direction was caused by the northward expansion of the aurora structure (gray arrow). This auroral structure gradually diminished without moving significantly, as shown in the bottom two images (0720:02 and 0720:30 UT).

The situation in Event 4 is similar to that in Event 6. In the topmost image (0727:10 UT), the angulated portion of the auroral structure is indicated by the gray arrow. At 0727:30 UT (second image), this structure shifted west-northwestward. Subsequently, as shown in the images captured at 0727:50 and 0728:02 UT, the auroral structure moved farther west-northwestward. The radar's field of view in this event cut across the auroral structure in a manner similar to that in Event 6.

The motion of the auroral structure in Event 5 is also similar to that in Event 6, even though the motion in the initial stage (images taken at 0736:27 and 0736:58 UT) was not clearly identified due to very strong emissions. At 0736:27 UT the strong aurora (gray arrow) began to intersect the radar's field of view. In the third image (0737:30 UT) the angulated portion of the auroral structure, which is the front edge of the moving auroral structure, is indicated by the gray arrow. A comparison of the images captured at 0737:30 UT and 0738:02 UT reveals that the auroral structure moved west-northwestward.

The images for Event 7 show that the narrow, long auroral structure was in motion. The images captured at 0755:07 and 0755:19 UT show that the initial increase in the auroral intensity in the radar's field of view (Figure 3c) is associated with the motion of the auroral structure. At 0755:42 UT, the direction of the radar beam passed through the central part of the auroral structure. At 0756:02 UT, when the ESR T_e was <2500 K, the radar's field of view was still passing through the auroral emission region.

Figures 4 and 5 indicate that in Events 2, and 4–7 among the defined seven events the mesoscale moving auroral structure passed through the direction of the radar beam. As described in Figure 3c, in these events, except for Event 2, the auroral emission sustained significant intensities even after the ESR T_e dropped. These common features are direct results of the motion of the mesoscale cusp auroral structure in the radar's field of view.

4. Discussion

4.1. Motion of Aurora and T_e Variations

In Figure 6 we illustrated a possible relationship between the motion of the auroral structure and the T_e variations, which is consistent with the common features of Events 4–7. The elongated shape shown at the top of the figure is the auroral emission region. The hatched region inside represents the T_e enhancement region, which was produced by electron precipitation. We assumed that the electron precipitation region moved in the direction indicated by the gray arrow. The small solid circle represents the relative position of the direction of the radar beam to the auroral structure at each of four different times of t_1, t_2, t_3, and t_4.
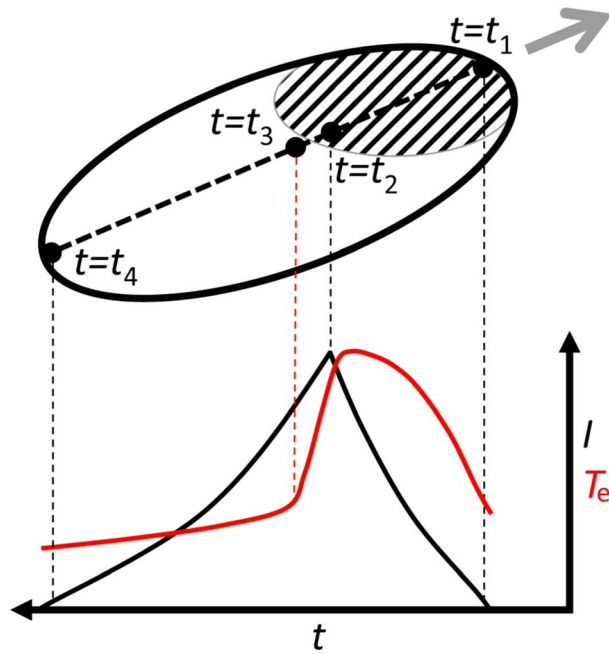
Figure 6. Schematic illustration showing a possible relation between the motion of the auroral structure and ESR T_e variations. An elongated shape shown at the top is the auroral emission region. The hatched region inside the auroral emission region represents the T_e enhancement region, which is produced by electron precipitation. The gray arrow indicates the direction in which the electron precipitation is moving. The small solid circle on the dotted line represents the relative position of the direction of the ESR beam to the auroral structure at each of four different times, $t = t_1$, t_2, t_3, and t_4. The bottom illustration represents the variations in the auroral intensity I (black) and the ESR T_e (red).

The direction of the radar beam was fixed; the difference in these points is due to simply the motion of the structure. The bottom illustration represents the variations in the auroral intensity I and the ESR T_e (shown in red).

The position labeled t_1 in the auroral structure represents the case in which the auroral structure just began to intersect the radar beam. The position labeled t_2 indicates the case in which the auroral intensity was the maximum when observed along the dotted line. This is schematically represented in the illustration at the bottom of the figure. This is not necessarily the maximum intensity point in the two-dimensional structure. We have illustrated the maximum ESR T_e simply near the maximum auroral intensity because the time resolution of ESR T_e (30 s) is very low compared with that of the aurora observation (4 s).

The position labeled t_3 represents the time at which the steep drop in T_e was observed. Because the drop in T_e value indicates the absence of substantial electron precipitation at this point, we have determined the region of electron precipitation (shaded region) so as to not include this position ($t = t_3$) in the electron precipitation region. Admittedly, the T_e enhancements may be delayed from the electron precipitation, but this delay is usually <30 s, which is the integration time of the ESR data. The numerical model by *Sadler et al.* [2012] shows that the electron temperatures are enhanced significantly about 20 s after the electron precipitation. The position labeled t_4 shows the case in which the auroral intensity diminished sufficiently and was close to the background level.

4.2. Equation of Continuity of O(^1D) in the Moving Cusp Aurora

To better understand the relationship summarized in Figure 6, we considered the volume emission rate for the auroral intensity. The auroral intensity I can be expressed as the integral of the volume emission rate ε along the line of sight:

$$I = 10^{-6} \int \varepsilon(x, y, z, t) \, dl, \tag{1}$$

where ε represents the three-dimensional distribution of the volume emission rate for the 630.0 nm emission, expressed in $cm^{-3} s^{-1}$; dl is the line element in centimeters; I is the intensity expressed in Rayleigh (R, 10^6 photons $cm^{-2} s^{-1}$); and ε is a function of time t and spatial parameters x, y, and z. We analyzed the auroral intensity data obtained in the direction of the radar beam, i.e., the elevation angle of 82° (Figure 3c). Because this elevation angle is approximately vertical upward, the integral along the line in (1) can be approximated as the integral along the vertical upward line. We then considered the vertical profiles, i.e., the altitude profiles of ε, below.

The model proposed by *Rees and Roble* [1986] indicates that the altitude profile of the normalized volume emission rate of the 630.0 nm radiation for incident Maxwellian electron-energy spectra with a characteristic energy of 100 eV peaks at an altitude of approximately 240 km. A recent study by *Taguchi et al.* [2015b] shows

that the electron precipitation features at approximately 100 eV are very similar between the moving cusp aurora in the initial stage and that in the final stage. It is reasonable to assume that the features of the electron precipitation do not change significantly at least during a brief period of a few minutes while the radar beam passes through the entire structure of the moving cusp aurora. On the basis of these two studies, we suggest that the constant distribution of the volume emission rate, which peaks at a certain altitude, exists for a brief period of observation.

The altitude profiles of ε decrease rapidly below and above the maximum altitude [*Rees and Roble*, 1986] even though its decrease is more rapid at lower altitudes owing to the effect of collisional quenching. For this type of distribution, the maximum value can be almost proportional to the integral of the function. For example, when we take a Gaussian function form, i.e., $\varepsilon = \varepsilon_M \exp(-(z - z_M)^2/(2h)^2)$, where z is the altitude, z_M is the altitude for the maximum ε_M, and h is the profile width of the Gaussian function, the integral of this function from $z = 0$ to $z = \infty$ gives $\sqrt{\pi}\varepsilon_M h$. This shows that ε_M, i.e., the maximum value of ε, is exactly proportional to the integral value. Under these circumstances, the auroral intensity can be regarded as being roughly proportional to the maximum value of ε and therefore to the number density of $O(^1D)$ at the altitude with the maximum ε; i.e., $I \propto n_M$, where I is the auroral intensity and n_M represents the number density of $O(^1D)$ at the altitude at which the maximum ε occurs. We then considered the continuity equation for n_M. In the following continuity equation,

$$\frac{\partial n_M}{\partial t} + \nabla \cdot (n_M \mathbf{v}) = P - L,\tag{2}$$

$\mathbf{v}$ represents the velocity of $O(^1D)$; P represents the production rate at altitude z_M for the maximum ε, which is associated with electron precipitation; and L is the loss rate at $z = z_M$. This loss rate can be expressed by n_M/τ_M, where τ_M is the lifetime of $O(^1D)$ at that altitude. In (2), P, which is related to the motion of the electron precipitation region, might be expressed by an appropriate function of spatial parameters x and y in the horizontal plane and time t. However, we rewrote (2) as the following equation to describe the temporal variations at a fixed position $(x, y, z) = (x_0, y_0, z_M)$ to explain the temporal variations obtained in Figure 3c:

$$\frac{\partial n_M(x_0, y_0, z_M, t)}{\partial t} + \frac{n_M(x_0, y_0, z_M, t)}{\tau_M}$$
$$= P(x_0, y_0, z_M, t) - [\nabla \cdot (n_M(x, y, z, t)\mathbf{v}(x, y, z, t))]_{\substack{x = x_0 \\ y = y_0 \\ z = z_M}}\tag{3}$$

The production rate at the fixed position, $P(x_0, y_0, z_M, t)$, should have significant values only during the interval in which the region of electron precipitation passes through $(x, y) = (x_0, y_0)$; this value should be zero before and after the interval. On the other hand, the $\nabla \cdot (n\mathbf{v})$ term, i.e., the second term on the right-hand side, is a nonzero term for a longer period than that of the nonzero interval of P because the velocity $\mathbf{v}$ of the neutral $O(^1D)$ is driven in a region larger than that of the electron precipitation. The electron precipitation responsible for the moving cusp aurora is accompanied by a twin-vortex plasma flow [e.g., *Southwood*, 1987; *Oksavik et al.*, 2004; *Taguchi et al.*, 2015a]. Specifically, intense electron precipitation occurs in one cell of the twin vortex [*Oksavik et al.*, 2004]. The velocity $\mathbf{v}$ of the neutral $O(^1D)$, which is driven by the plasma flow, is collocated roughly to the twin-vortex plasma flow. This indicates that the region in which the $\nabla \cdot (n\mathbf{v})$ term has nonzero values is larger than the electron precipitation region corresponding to one cell in the twin vortex.

Despite the fact that the $\nabla \cdot (n\mathbf{v})$ term may have nonzero values in a longer period than the nonzero interval of $P(x_0, y_0, z_M, t)$, the former is without doubt the secondary effect as compared with $P(x_0, y_0, z_M, t)$, which is the main source of the aurora. In the equations below, we assumed that the sum of the two terms on the right-hand side in (3) is approximately constant during the period in which the region of electron precipitation is passing through $(x, y) = (x_0, y_0)$ and that the sum is zero before and after that period. Taking the nonzero interval as $t = 0$ to $t = \tau_P$ and denoting the constant value as P_0, (3) can be expressed as

$$\frac{\partial n_M(t)}{\partial t} + \frac{n_M(t)}{\tau_M} = \begin{cases} P_0 & (0 \leq t \leq \tau_P) \\ 0 & (\text{otherwise}) \end{cases}.\tag{4}$$

These equations can be analytically solved; and the solution for $0 \leq t$ is
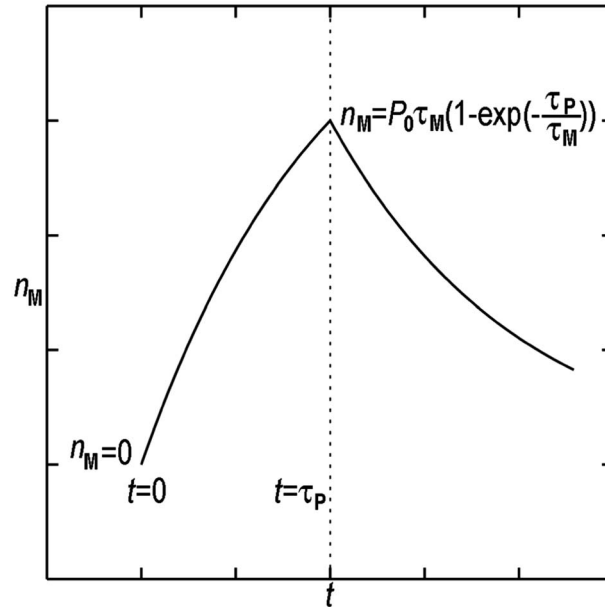
Figure 7. General profiles of equations (5) and (6) for n_M in an arbitrary unit. The n_M variation takes its maximum at $t = \tau_P$.

$$n_M(t) = P_0\tau_M\left(1 - \exp\left(-\frac{t}{\tau_M}\right)\right) \quad 0 \leq t \leq \tau_p \tag{5}$$

$$n_M(t) = P_0\tau_M\left(\exp\left(-\frac{t-\tau_p}{\tau_M}\right) - \exp\left(-\frac{t}{\tau_M}\right)\right) \quad \tau_p < t \tag{6}$$

In Figure 7, we illustrate the general profiles of (5) and (6) in an arbitrary unit. After $t = 0$, n_M increases and reaches its maximum at $t = \tau_P$. The maximum value of n_M,

$$n_M = P_0\tau_M\left(1 - \exp\left(-\frac{\tau_P}{\tau_M}\right)\right), \tag{7}$$

is expressed with the two characteristic times, τ_P and τ_M. Again, τ_P is the time representing the duration of the production, and τ_M is the lifetime of O(^{1}D), which characterizes the decay of the aurora. When the constant production ends, n_M begins to decrease exponentially. At $t = \tau_P + \tau_M$, n_M decreases to $1/e$ of the maximum value (7). The decreasing phase, i.e., $\tau_P < t$, corresponds to the stage after the passage of the electron precipitation region.

4.3. Comparison of Model With Observation

Figure 8 shows the result of the least squares fitting of (5) and (6) to the variations of the observed auroral intensities for Event 4. The black dots indicate the auroral intensities observed at the 4 s interval, and the red curve is the result of the least squares fitting. The horizontal axis represents time t expressed in seconds. The left vertical line represents the start time of the auroral enhancements for Event 4, i.e., 0727:10 UT, which is defined in Figure 3c. The right vertical line shows 0729:29 UT. At the latter time, the auroral intensity returned to a value close to that obtained at the start of the auroral intensification (left vertical line). We determined $t = 0$ as 4 s before the start of the auroral enhancements (0727:06 UT = 0726:10 UT − 4 s), and we took the auroral intensity at $t = 0$ as the baseline. Fitting was performed by using the data obtained after subtracting this baseline from the values observed between the two times given above (shown as vertical lines). We determined τ_P and τ_M with a time resolution of 10 s.

The result of the fitting shows that $\tau_P = 60$ s, $\tau_M = 80$ s, and $fP_0 = 40$ R s^{-1}. In these results, we introduced the ratio f, which represents the proportionality of (5) or (6) to the actual auroral intensity. Figure 8 shows that the fitting is reasonably good. The estimated lifetime of O(^{1}D), $\tau_M = 80$ s, is in the expected range, i.e., 30–80 s [e.g., *Sipler and Biondi*, 1972]. The estimated duration of the production, $\tau_P = 60$ s, is somewhat longer
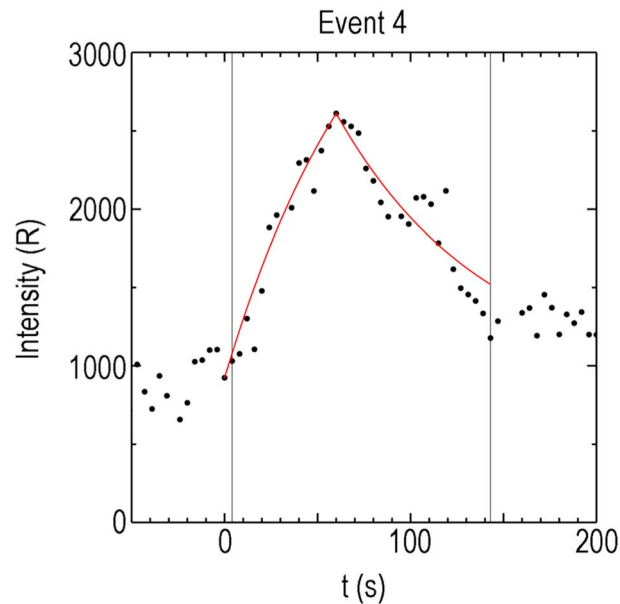
Figure 8. Result of least squares fitting (red curves) of equations (5) and (6) to the observed values (dots) for Event 4. The left vertical line represents the time for the start of the auroral enhancements, i.e., 0727:10 UT, which is defined in Figure 3c, and the right vertical line shows 0729:29 UT.

than the ESR one-integration time of 30 s during which T_e was sharply enhanced (Event 4 in Figures 3b and 3c). However, that difference is not significant considering that the time resolution of the ESR data is 30 s. When we took $1 \, \text{km s}^{-1}$ as the typical speed of the electron precipitation region, as described in section 1, the horizontal extent of the electron precipitation region traversed by the radar beam was 60 km ($= 1 \, \text{km s}^{-1} \times \tau_P$). Although no electron precipitation was observed on the backside of that region, auroral emission did occur. Thus, the characteristic length of this extended part at the back is comparable to the horizontal scale of the electron precipitation region for this event. We will discuss the area ratio of the auroral emission region to the electron precipitation region later.

As shown in section 3.3, the variations in the auroral intensity in Events 1 and 3 were not the result of simple motion of the mesoscale auroral structure, and we did not perform fitting. For Event 2, we obtained $\tau_P = 10 \, \text{s}$ and $\tau_M = 50 \, \text{s}$. The latter again fits in the range implied by *Sipler and Biondi* [1972]. For Events 5–7, we did not perform fitting because the data around the maximum intensity were not correctly observed, as shown in Figure 3c. However, we can infer the time for the maximum intensity to an accuracy of 15 s for Event 7 because the interval of the "flat" intensities was relatively short (15 s). For the other two events, the interval was rather long at 59 s and 95 s, respectively. When taking $t = 0$ for Event 7 to be 0755:03 UT ($= 0755:07 \, \text{UT} - 4 \, \text{s}$) in a manner similar as that for Event 4, we can infer that τ_P is 32 s ($= 0755:35 \, \text{UT} - 0755:03 \, \text{UT}$) to 47 s ($= 0755:50 \, \text{UT} - 0755:03 \, \text{UT}$). This duration is consistent with the ESR two-integration time of 60 s during which T_e was sharply enhanced (Event 7 in Figures 3b and 3c).

4.4. Horizontal Profile of the Moving Cusp Aurora

Finally, we discuss the horizontal extension of the auroral emission region. In the previous subsections, we discussed the temporal change in $O(^1D)$ density and the auroral intensity at a fixed position, and we attributed these variations to the passage of the electron precipitation region. We assume here that the speed and size of the electron precipitation region is constant for a brief period such as a few minutes. We then substitute $t = L/V_P$ in (5) and (6), where V_P is the constant speed of the electron precipitation region and L is the length from the front edge of the electron precipitation region to the back. We express τ_P as L_P/V_P, where L_P is the length of the electron precipitation region from its front edge to the trailing edge along its moving direction. As described in section 4.3, we introduced the ratio f to explain I instead of n_M. The following equations can be obtained for I:
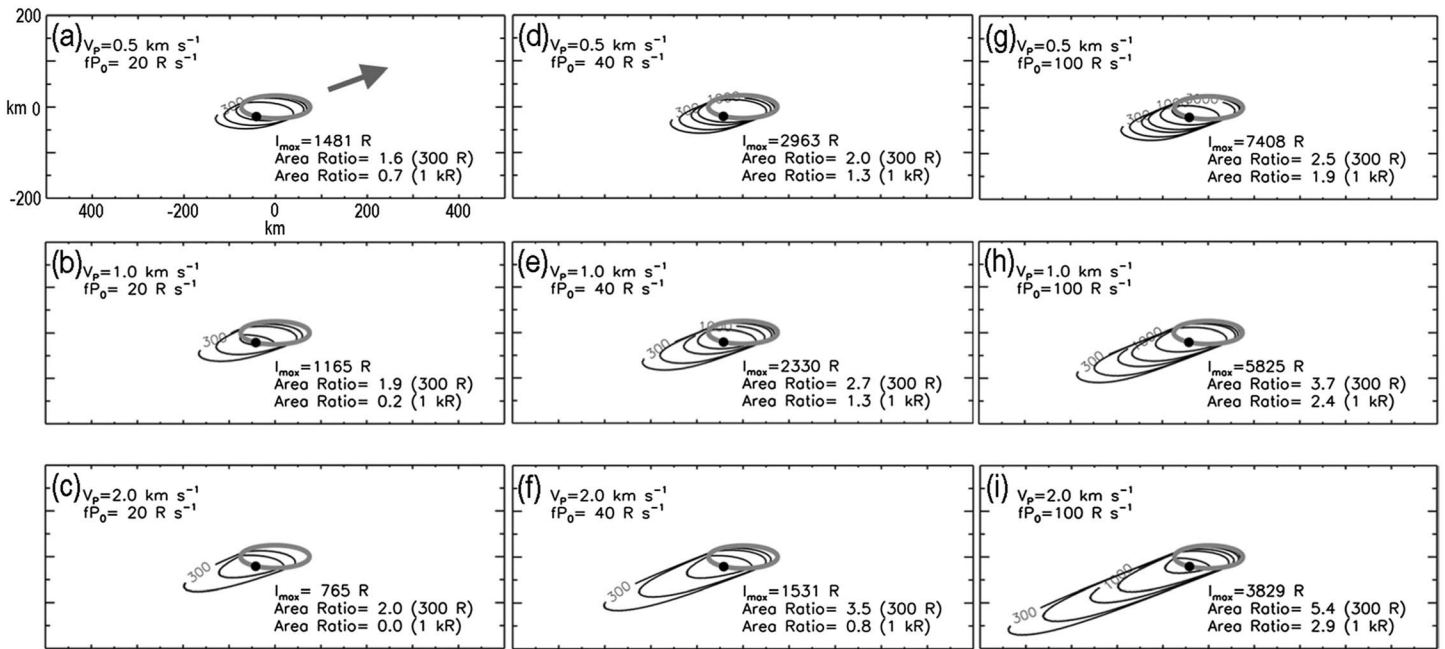
Figure 9. Calculation results of the horizontal extension of the 630 nm aurora emission region for nine conditions. (a–i) Each case has different values for two input parameters V_P and fP_0. The values of these parameters are indicated at the top left of each figure. The gray arrow in Figure 9a indicates the assumed direction of the moving electron precipitation region (gray elliptical shape). The small solid circle represents the location of the maximum auroral intensity. The contours show the intensities of 300 R, 500 R, 1 kR, 1.5 kR, 3.0 kR, and 6.0 kR. The obtained maximum intensity and the area ratio of the calculated auroral emission region, which is characterized by 300 R or 1 kR, relative to the electron precipitation region are shown at the bottom right.

$$I = fP_0\tau_M\left(1 - \exp\left(-\frac{L}{V_P\tau_M}\right)\right) \quad 0 \leq L \leq L_P \tag{8}$$

$$I = fP_0\tau_M\left(\exp\left(-\frac{L - L_P}{V_P\tau_M}\right) - \exp\left(-\frac{L}{V_P\tau_M}\right)\right) \quad L_P < L. \tag{9}$$

Once the electron precipitation region and the direction of its motion have been determined, we can define various L lines in which the origins are located at any point at the forward edge of the electron precipitation region. We can calculate the variations of the auroral intensity along each of those L lines by using (8) and (9), and we can then obtain the two-dimensional distribution of I. For the shape of the electron precipitation region, we assumed an elliptical shape in which the major and minor axes were 150 km and 50 km, respectively. These dimensions are consistent with previous observations. *Taguchi et al.* [2015a] adopted the area delineated by a semicircle with a diameter of 150 km for the mesoscale upward field-aligned current region, which is thought to be collocated with the electron precipitation region associated with the moving cusp auroral structure. Collocation of intense electron precipitation with a mesoscale upward field-aligned current in an event was also reported by *Taguchi et al.* [1993] (e.g., 0251:32 UT to 0251:40 UT in Plate 1 of that work). This interval of 8 s corresponds to the length of 64 km at the *F* region height.

Figure 9 shows the results from the calculation of nine cases for $\tau_M = 80$ s. In each figure, the assumed region of electron precipitation is represented by a gray line. The gray arrow in Figure 9a indicates that this region is moving along 22.5° from the horizontal axis. The horizontal axis represents a length of 1000 km, and the vertical axis shows a length of 400 km, as also indicated in Figure 9a. The nine cases are characterized by three values of speed, $V_P = 0.5$, 1.0, and 2.0 km s^{-1}, and three values of $fP_0 = 20$, 40, and 100 R s^{-1}. For fP_0, which represents the strength of the production rate, we used the value obtained from the data fitting (Figure 7), 40 R s^{-1} plus its one-half and 2.5-fold values (20 R s^{-1} and 100 R s^{-1}) for simplicity. The calculated maximum intensity is shown at the bottom right of each plot. The location of the maximum intensity is represented by the small solid circle. In each case, the black contours represent the auroral intensities. The outermost contour represents 300 R. At the bottom right, we also show the area ratio of the auroral emission region defined by

300 R and 1 kR to the electron precipitation region. It should be noted that we do not intend to explain the seven events shown in Figure 5 by the calculation of the nine cases shown in Figure 9.

Comparison of the results shown in Figures 9a–9c, 9d–9f, and 9g–9i show that as the speed of the electron precipitation region increases, the auroral emission region is elongated. This tendency is independent of the value of fP_0. The results also show that as the speed of the electron precipitation region decreases, the maximum auroral intensity becomes stronger regardless of the value of fP_0. In all cases, the maximum auroral intensity occurs at a point along the trailing edge of the electron precipitation region. This point is located near the center of the entire structure of the auroral emission with an intensity of either 300 R or 1 kR, although in the case of Figure 9i the maximum point is far from the rear boundary of the auroral emission. This indicates the possibility that the motion of the electron precipitation can be estimated from the motion of the point at which the auroral intensity is the maximum within the entire auroral structure [*Taguchi et al.*, 2015a]. For the cases of typical speed, $V_P = 1\ km\ s^{-1}$ (Figures 9b, 9e, and 9h), the area of the auroral emission is about 2 to 4 times that of the electron precipitation region when the area of auroral emissions is characterized by an intensity of 300 R. If the area of auroral emissions is characterized by an intensity of 1 kR, the area ratio is smaller.

In Figure 9 we assumed the size of the electron precipitation region and the direction of its motion. When we consider the case in which the elliptical region of electron precipitation moves along the horizontal axis rather than 22.5° from the horizontal axis, the maximum intensity becomes stronger, and the auroral emission region is more elongated than those in Figure 9 owing to the larger L_P in (8) and (9). On the other hand, if the region moves along the vertical axis, the maximum intensity becomes weaker, and the auroral emission region is smaller than those in Figure 9. The ratio of the maximum auroral intensities for these two cases can be obtained from (8) or (9) as follows:

$$\frac{I_h}{I_v} = \frac{1 - \exp\left(-\frac{L_{P\max}}{V_P \tau_M}\right)}{1 - \exp\left(-\frac{L_{P\min}}{V_P \tau_M}\right)}, \tag{10}$$

where I_h and I_v represent the maximum auroral intensities for the cases in which the electron precipitation region moves along the horizontal and vertical axes, respectively, and $L_{P\max}$ and $L_{P\min}$ show the length of the major and minor axis, respectively.

When $L_{P\max} = 150\ km$, $L_{P\min} = 50\ km$, $V_P = 1.0\ km\ s^{-1}$, and $\tau_M = 80\ s$ are used in (10), we can obtain $I_h/I_v \sim 2$. This indicates that the direction of the motion of the electron precipitation region is also associated with the distribution of the auroral intensity. This indicates that the area of the electron precipitation itself, the speed and direction of the motion of that region, and the production rate control the size and shape of the 630.0 nm auroral emissions, which extend behind the electron precipitation region. That is, it is difficult to determine the part in which the electron precipitation occurs in the red line mesoscale aurora structure from only the information of the location of the maximum auroral intensity in a single auroral image. However, if we can estimate the speed and direction of the electron precipitation region from sequences of auroral images, we can better understand the horizontal extent of the electron precipitation in the red line auroral structure.

The results from our calculation agree with some of the features obtained in past research. *Sandholt et al.* [1986] showed that highly longitudinal extension of the 630.0 nm aurora is often observed with longitudinal movement. The longitudinal motion of the aurora appears when IMF is dawnward or duskward [e.g., *Sandholt et al.*, 1986]. Under these IMF conditions, the convection in the cusp is strong in the longitudinal direction and tends to be fast [e.g., *Knipp et al.*, 2011; *Wilder et al.*, 2013]. Along with rapid convection, the electron precipitation region will move rapidly in the longitudinal direction. Our model shows that as the speed of the electron precipitation region increases, the auroral emission region is elongated, which creates a highly longitudinal extension of the aurora.

Fasel et al. [1992] reported phenomena in which poleward moving auroral structures have multiple intensifications during their movement. Our model suggests that the auroral intensity becomes stronger as the speed of the electron precipitation region decreases. If the convection slows down in the cusp, rebrightening of the moving aurora may occur. In fact, *Fasel* [1995] reported that some moving auroral structures slow down and stop while continuing to rebrighten.

By examining a moving cusp aurora structure which has a typical horizontal scale of roughly 100 km × 200 km, *Taguchi et al.* [2015a] determined that the maximum 630.0 nm intensity of that auroral structure occurs immediately behind the moving *F* region-enhanced electron density volume created by precipitating electrons. This spatial relationship agrees with the distribution obtained from our calculation.

We have suggested that the velocity of the electron precipitation region is important in determining the maximum intensity in the auroral structure and the horizontal extension of the auroral emission region behind the electron precipitation region. To extract the horizontal extension of the auroral emission region from all-sky image data more precisely, we need to consider the altitude profiles of the auroral emissions as well as the distribution of velocity $\mathbf{v}$ of the neutral $O(^1D)$ and the temporal variations of the production rate, which have not been considered in our estimates. The altitude for the 630.0 nm auroral emissions in the cusp may range from 200 km to at least 400 km.

5. Conclusions

By investigating the all-sky images obtained with a time resolution of 4 s and comparing the results with the 30 s integrated T_e measured simultaneously by ESR, we have shown the manner in which the moving cusp auroral structure passed though the ESR's field of view during 0700–0800 UT on 27 November 2011. In four of seven events, the radar's field of view cut across the central part of the moving mesoscale auroral structures. When the front edge of the auroral structure intersected the radar's field of view, the ESR electron temperature increased rapidly. A few minutes later, the electron temperature dropped to the background level, indicating that the electron precipitation region has passed through the radar's field of view. At that time, the auroral emission in the radar's field of view decreased but still had significant intensities without reaching the background level. These results provide direct evidence demonstrating that the moving red line cusp auroral emission occurs behind the electron precipitation region as well as in that region. That is, a moving cusp aurora does not have electron precipitation in its rear half. Our semiquantitative modeling based on the equation of continuity of the density of the excited atomic oxygen has shown that as the speed of the electron precipitation region increases, the auroral emission region is elongated. Moreover, our model shows that as the speed of the electron precipitation region decreases, the auroral intensity becomes stronger, and that the maximum auroral intensity occurs at a point along the trailing edge of the electron precipitation region. Therefore, the velocity of the electron precipitation region is an important factor for determining the distribution of 630.0 nm aurora emissions.

References

Carlson, H. C., K. Oksavik, and J. I. Moen (2013), Thermally excited 630.0 nm $O(^1D)$ emission in the cusp: A frequent high-altitude transient signature, *J. Geophys. Res. Space Physics*, *118*, 5842–5852, doi:10.1002/jgra.50516.

Doe, R. A., J. D. Kelly, and E. R. Sánchez (2001), Observations of persistent dayside *F* region electron temperature enhancements associated with soft magnetosheathlike precipitation, *J. Geophys. Res.*, *106*(A3), 3615–3630, doi:10.1029/2000JA000186.

Fasel, G. J. (1995), Dayside poleward moving auroral forms: A statistical study, *J. Geophys. Res.*, *100*(A7), 11,891–11,905, doi:10.1029/95JA00854.

Fasel, G. J., J. I. Minow, R. W. Smith, C. S. Deehr, and L. C. Lee (1992), Multiple brightening of transient dayside auroral forms during oval expansions, *Geophys. Res. Lett.*, *12*, 2429–2432, doi:10.1029/92GL02103.

Haerendel, G., G. Paschmann, N. Sckopke, H. Rosenbauer, and P. C. Hedgecock (1978), The frontside boundary layer of the magnetosphere and the problem of reconnection, *J. Geophys. Res.*, *83*(A7), 3195–3216, doi:10.1029/JA083iA07p03195.

Hosokawa, K., S. Taguchi, Y. Ogawa, and T. Aoki (2013a), Periodicities of polar cap patches, *J. Geophys. Res. Space Physics*, *118*, 447–453, doi:10.1029/2012JA018165.

Hosokawa, K., S. Taguchi, Y. Ogawa, and J. Sakai (2013b), Two-dimensional direct imaging of structuring of polar cap patches, *J. Geophys. Res. Space Physics*, *118*, 6536–6543, doi:10.1002/jgra.50577.

Hosokawa, K., S. Taguchi, and Y. Ogawa (2016a), Edge of polar cap patches, *J. Geophys. Res. Space Physics*, *121*, 3410–3420, doi:10.1002/2015JA021960.

Hosokawa, K., S. Taguchi, and Y. Ogawa (2016b), Periodic creation of polar cap patches from auroral transients in the cusp, *J. Geophys. Res. Space Physics*, *121*, 5639–5652, doi:10.1002/2015JA022221.

Knipp, D., S. Eriksson, L. Kilcommons, G. Crowley, J. Lei, M. Hairston, and K. Drake (2011), Extreme Poynting flux in the dayside thermosphere: Examples and statistics, *Geophys. Res. Lett.*, *38*, L16102, doi:10.1029/2011GL048302.

Kozyra, J. U., C. E. Valladares, H. C. Carlson, M. J. Buonsanto, and D. W. Slater (1990), A theoretical study of the seasonal and solar cycle variations of stable auroral red arcs, *J. Geophys. Res.*, *95*, 12,219–12,234, doi:10.1029/JA095iA08p12219.

Lockwood, M., and H. C. Carlson Jr. (1992), Production of polar cap electron density patches by transient magnetopause reconnection, *Geophys. Res. Lett.*, *19*, 1731–1734, doi:10.1029/92GL01993.

Lockwood, M., H. C. Carlson Jr., and P. E. Sandholt (1993), Implications of the altitude of transient 630-nm dayside auroral emissions, *J. Geophys. Res.*, *98*(A9), 15,571–15,587, doi:10.1029/93JA00811.

Lockwood, M. P., E. Sandholt, S. W. H. Cowley, and T. Oguti (1989), Interplanetary magnetic field control of dayside auroral activity and the transfer of momentum across the dayside magnetopause, *Planet. Space Sci.*, *37*(11), 1347–1365, doi:10.1016/0032-0633(89)90106-2.

Moen, J., P. E. Sandholt, M. Lockwood, W. F. Denig, U. P. Løvhaug, B. Lybekk, A. Egeland, D. Opsvik, and E. Friis-Christensen (1995), Events of enhanced convection and related dayside auroral activity, *J. Geophys. Res.*, *100*(A12), 23,917–23,934, doi:10.1029/95JA02585.

Oksavik, K., J. Moen, and H. C. Carlson (2004), High-resolution observations of the small-scale flow pattern associated with a poleward moving auroral form in the cusp, *Geophys. Res. Lett.*, *31*, L11807, doi:10.1029/2004GL019838.

Rees, M. H., and R. G. Roble (1975), Observations and theory of the formation of stable auroral red arcs, *Rev. Geophys.*, *13*(1), 201–242, doi:10.1029/RG013i001p00201.

Rees, M. H., and R. G. Roble (1986), Excitation of $O(^1D)$ atoms in aurorae and emission of the [OI] 6300-A line, *Can. J. Phys.*, *64*(12), 1608–1613, doi:10.1139/p86-284.

Russell, C. T., and R. C. Elphic (1978), Initial ISEE magnetometer results—Magnetopause observations, *Space Sci. Rev.*, *22*, 681–715, doi:10.1007/BF00212619.

Sadler, F. B., M. Lessard, E. Lund, A. Otto, and H. Lühr (2012), Auroral precipitation/ion upwelling as a driver of neutral density enhancement in the cusp, *J. Atmos. Sol. Terr. Phys.*, *87–88*, 82–90, doi:10.1016/j.jastp.2012.03.003.

Sakai, J., K. Hosokawa, S. Taguchi, and Y. Ogawa (2014), Storm-time enhancements of 630.0-nm airglow associated with polar cap patches, *J. Geophys. Res. Space Physics*, *119*, 2214–2228, doi:10.1002/2013JA019197.

Sandholt, P. E., C. S. Deehr, A. Egeland, B. Lybekk, R. Viereck, and G. J. Romick (1986), Signatures in the dayside aurora of plasma transfer from the magnetosheath, *J. Geophys. Res.*, *91*(A9), 10,063–10,079, doi:10.1029/JA091iA09p10063.

Sandholt, P. E., M. Lockwood, T. Oguti, S. W. H. Cowley, K. S. C. Freeman, B. Lybekk, A. Egeland, and D. M. Willis (1990), Midday auroral breakup events and related energy and momentum transfer from the magnetosheath, *J. Geophys. Res.*, *95*(A2), 1039–1060, doi:10.1029/JA095iA02p01039.

Sipler, D. P., and M. A. Biondi (1972), Measurements of $O(^1D)$ quenching rates in the F region, *J. Geophys. Res.*, *77*(31), 6202–6212, doi:10.1029/JA077i031p06202.

Southwood, D. J. (1987), The ionospheric signature of flux transfer events, *J. Geophys. Res.*, *92*(A4), 3207–3213, doi:10.1029/JA092iA04p03207.

Suzuki, S., S. Taguchi, K. Hosokawa, M. R. Collier, T. E. Moore, H. U. Frey, and S. B. Mende (2008), Conjugate observations of ENA signals in the high-altitude cusp and proton auroral spot in the low-altitude cusp with IMAGE spacecraft, *Geophys. Res. Lett.*, *35*, L13103, doi:10.1029/2008GL034543.

Taguchi, S., M. Sugiura, J. D. Winningham, and J. A. Slavin (1993), Characterization of the IMF B_Y-dependent field-aligned currents in the cleft region based on DE 2 observations, *J. Geophys. Res.*, *98*, 1393–1407, doi:10.1029/92JA01014.

Taguchi, S., S. Suzuki, K. Hosokawa, Y. Ogawa, A. S. Yukimatu, N. Sato, M. R. Collier, and T. E. Moore (2009), Moving mesoscale plasma precipitation in the cusp, *J. Geophys. Res.*, *114*, A06211, doi:10.1029/2009JA014128.

Taguchi, S., K. Hosokawa, Y. Ogawa, T. Aoki, and M. Taguchi (2012), Double bursts inside a poleward-moving auroral form in the cusp, *J. Geophys. Res.*, *117*, A12301, doi:10.1029/2012JA018150.

Taguchi, S., K. Hosokawa, and Y. Ogawa (2015a), Three-dimensional imaging of the plasma parameters of a moving cusp aurora, *J. Atmos. Sol. Terr. Phys.*, *133*, 98–110, doi:10.1016/j.jastp.2015.08.012.

Taguchi, S., K. Hosokawa, and Y. Ogawa (2015b), Investigating the particle precipitation of a moving cusp aurora using simultaneous observations from the ground and space, *Prog. Earth Planet. Sci.*, *2*, 11, doi:10.1186/s40645-015-0044-7.

Vorobjev, V. G., G. Gustafsson, G. V. Starkov, Y. I. Feldstein, and N. F. Shevnina (1975), Dynamics of day and night aurora during substorms, *Planet. Space Sci.*, *23*, 269–278, doi:10.1016/0032-0633(75)90132-4.

Watermann, J., D. Lummerzheim, O. de laBeaujardière, P. T. Newell, and F. J. Rich (1994), Ionospheric footprint of magnetosheathlike particle precipitation observed by an incoherent scatter radar, *J. Geophys. Res.*, *99*, 3855–3867, doi:10.1029/93JA01995.

Wilder, F. D., S. Eriksson, H. Korth, J. B. H. Baker, M. R. Hairston, C. Heinselman, and B. J. Anderson (2013), Field-aligned current reconfiguration and magnetospheric response to an impulse in the interplanetary magnetic field B_Y component, *Geophys. Res. Lett.*, *40*, 2489–2494, doi:10.1002/grl.50505.